Electrochimica Acta 255 (2017) 168–178

Contents lists available at ScienceDirect

Electrochimica Acta

journal homepage: www.elsevier.com/locate/electacta

Three-Dimensional Cyclic Voltammetry Simulations of EDLC Electrodes Made of Ordered Carbon Spheres

Bing-Ang Mei, Laurent Pilon*

Mechanical and Aerospace Engineering Department, Henry Samueli School of Engineering and Applied Science, University of California, Los Angeles - Los Angeles, CA 90095, USA

ARTICLE INFO

Article history:
Received 15 May 2017
Received in revised form 26 July 2017
Accepted 11 September 2017
Available online 20 September 2017

Keywords:
EDLC
3D structure
Ordered carbon spheres
electrode packing arrangement

ABSTRACT

This study aims to investigate the effect of electrode nanoarchitecture on the performance of electric double layer capacitor (EDLC) porous electrodes consisting of highly-ordered monodisperse spherical carbon nanoparticles. To do so, cyclic voltammograms, reproducing three-electrode measurements, were numerically generated for electrodes with different thicknesses and nanoparticle diameters arranged in either simple cubic (SC) or face-centered cubic (FCC) packing structure. The transient three-dimensional simulations of interfacial and transport phenomena in the porous electrodes were based on a continuum model accounting for (1) binary symmetric electrolytes with finite ion size, (2) electric field-dependent dielectric constant of the electrolyte, (3) the Stern layer at the electrode/electrolyte interface, along with (4) Ohmic potential drop in the electrode. For both FCC and SC packing structures, the areal capacitance (in μF/cm^2) increased with decreasing sphere diameter. In addition, for a given sphere diameter, FCC packing featured larger equilibrium capacitance than SC packing. These observations were attributed to larger electric field at the carbon sphere surface for smaller spheres and/or FCC packing. In all cases, the areal capacitance remained constant at low scan rates but decreased beyond a critical scan rate. The latter rate-dependent regime was reached at lower scan rates for thicker electrodes due to resistive losses across the electrode. Interestingly, limitation due to ion diffusion through the porous electrode was not observed. Finally, dimensional analysis was performed by scaling the CV cycle period by the time scale for electron transport in the electrode. This study illustrates powerful numerical simulation tools that can be used to select materials and electrolytes and to design and optimize EDLC electrodes.

1. Introduction

Electric double layer capacitors (EDLCs) have drawn significant attention due to their promise as electric energy storage systems [1–4]. They are typically made of two porous carbon electrodes immersed in a concentrated liquid electrolyte [5–19]. They store electric energy physically in the electric double layer forming at a porous electrode/electrolyte interface. They feature fast charging and discharging rates and thus large power density. They also have long cycle life thanks to reversible EDL formation. They can be used in various applications including regenerative braking, digital telecommunication, and dynamic stabilization of the utility grid [1–4,20].

The performance of EDLCs is greatly influenced by the morphology of the electrodes [2,21–24,12,25–27,11,28,29]. Experimental measurements have been reported for different porous carbon electrodes made of ordered or disordered carbon spheres [2,21–24,12,25–27,11,28,29]. However, experiments to improve electrode or device performance have been performed by trial and error, albeit informed by physical intuition. Unfortunately, this approach can be time-consuming and costly, and intuition is made difficult by the large number of parameters and the different competing interfacial and transport phenomena. On the other hand, most previous numerical models treated the electrode microarchitecture as homogeneous with some effective macroscopic properties determined from effective medium approximations (EMAs) and assumed transport phenomena as one-dimensional [30–59]. These models typically do not account for the detailed porous electrode architecture [30–59].

This paper aims to investigate the effect of electrode nanoarchitecture on the performance of EDLC porous electrodes. To do so, a three-dimensional modeling tool was developed to simulate interfacial and transport phenomena in porous electrodes filled with electrolyte under dynamic charging and discharging. In fact,

---

* Corresponding author. Tel.: +1 310 206 5598; fax: +1 310 206 4830.
E-mail address: pilon@seas.ucla.edu (L. Pilon).

http://dx.doi.org/10.1016/j.electacta.2017.09.060

cyclic voltammograms of three-electrode systems were reproduced numerically for various electrode dimensions and morphologies. This could accelerate the design and optimization of EDLC electrodes to maximize their energy and power densities.

Nomenclature

a	Effective ion diameter (nm)
c	Ion concentration (mol/L)
C	Capacitance (μF/cm^2 or F/g)
d	Diameter of the carbon sphere (nm)
D	Diffusion coefficient of ions in electrolyte (m^2/s)
E	Magnitude of the electric field (V/m)
e	Elementary charge, $e = 1.602 \times 10^{-19}$ C
F	Faraday constant, $F = eN_A = 9.648 \times 10^4$ C mol^{-1}
H	Stern layer thickness (nm)
i	Index of the carbon spheres
j	Magnitude of current density (A/m^2 or A/g)
L	Half of interelectrode distance (nm)
L_s	Thickness of the carbon current collector (nm)
L_c	Total thickness of the electrode (nm)
M_c	Molecular mass of the electrode (kg)
$\mathbf{n}$	Normal vector of a surface
N	Number of the carbon spheres
n	Refractive index of the electrolyte
n_c	Cycle number
n_e	Number of free electrons per atom
N_A	Avogadro number, $N_A = 6.022 \times 10^{23}$ mol^{-1}
N_i	Ion flux of species i (mol m^{-2}s^{-1})
Q	Charge stored (C)
$\mathbf{r}$	Location in three-dimensional space (nm)
$\mathbf{r}_{C/E}$	Location of the current collector/electrolyte interface (nm)
$\mathbf{r}_{E/E}$	Location of the electrode/electrolyte interface (nm)
$\mathbf{r}_{cl}$	Location of the electrolyte centerline (nm)
$\mathbf{r}_H$	Location of the Stern/diffuse layer interface (nm)
R_u	Universal gas constant, $R_u = 8.314$ J mol^{-1}K^{-1}
T	Local temperature (K)
t	Time (s)
u_e	Drift velocity of electrons in the electrode (m/s)
v	Scan rate of the cyclic voltammetry (V/s)
z	Ion valency

Greek symbols

α	Parameter for electron transport in the electrode
ε_0	Vacuum permittivity, $\varepsilon_0 = 8.854 \times 10^{-12}$ F m^{-1}
ε_r	dielectric constant of the electrolyte
ρ_c	Density of the electrode (kg/m^3)
σ_c	Electrical conductivity of carbon electrode (S/m)
τ_D	Time scale for ion transport in the electrolyte (s)
τ_e	Time scale for electron transport in the electrode (s)
τ_{CV}	Cycle period (s)
ψ	Electric potential (V)
ψ_{min}, ψ_{max}	Minimum and maximum of the potential window (V)
ψ_s	Imposed potential (V)

Superscripts and subscripts

*	Refers to dimensionless variable
BET	Refers to the surface area of electrode/electrolyte interface
fp	Refers to footprint surface
g	Refers to gravimetric variables
∞	Refers to bulk electrolyte
i	Refers to ion species i
n	Refers to normal component of a variable
St	Refers to Stern layer

2. Background

2.1. Experimental studies

Experimental studies have established that the specific surface area (in m^2/g) as well as the porous architecture of the carbon electrodes affect the performance of EDLCs [2,21–24,12,25–27,11,28,29]. For example, Vix-Guterl et al. [12] studied the performance of EDLC with porous carbon electrodes made from propylene (CPr), pitch (CP), and sucrose (CS) in 1 M aqueous H_2SO_4, 6 M aqueous KOH, and 1 M $(C_2H_5)_4NBF_4/CH_3CN$ electrolytes. Electrodes made of CPr and CP had mesopores with specific surface area of about 900 m^2/g and specific pore volume of 0.6 cm^3/g while electrodes made of CS had additional micropores resulting in larger specific surface area of about 2000 m^2/g and specific pore volume of 1.1 cm^3/g. The gravimetric capacitances of CS electrodes were 200 F/g (areal capacitance 10 μF/cm^2) and 110 F/g (areal capacitance 5.5 μF/cm^2) in aqueous and organic electrolyte, respectively. These were larger than the gravimetric capacitances of CPr and CP electrodes of about 100 F/g and 60 F/g in aqueous and organic electrolyte, respectively. The difference was attributed to the larger specific surface area. In addition, Kim et al.[22] assembled an EDLC device made of two identical electrodes consisting of monodisperse porous carbon spheres about 500 nm in diameter either three-dimensional ordered in FCC packing or disordered with specific surface area of 1260 m^2/g, in 1 M aqueous Na_2SO_4 electrolyte. The CV curves for electrodes made of ordered carbon spheres retained a nearly rectangular shape for scan rates as fast as 1 V/s while those with disordered carbon spheres showed an increasingly resistive behavior as scan rate increased. In fact, the electrodes made of ordered carbon spheres had a gravimetric capacitance of 60 F/g (areal capacitance 4.76 μF/cm^2) which was about 50% larger than the capacitance of electrodes made of disordered carbon spheres.

2.2. Numerical studies

Various models and simulation methods have been developed to predict the performance of EDLCs [30–60]. RC circuit models consist of modeling an EDLC device by an electric circuit consisting of an arbitrary number of ideal capacitors and resistors [30–38]. These models require prior knowledge of electrical behavior and properties of EDLCs determined experimentally [35]. In addition, RC circuit models neglect ion diffusion and non-uniform ion concentrations in the electrolyte [36–38]. Moreover, two different RC circuit models may produce similarly acceptable impedance response. This suggests that fitted values of the resistances and capacitances in the RC circuit models provides “little or no direct information about the physical meaning of the elements for such models” [40]. Therefore, RC circuit models can be used to control the operation of specific EDLCs but not for designing and optimizing electrode morphology.

Alternatively, molecular simulations have been used extensively to simulate ion transport in the electrolyte near the electrode/electrolyte interface of EDLCs including Monte Carlo (MC) simulations [41,42] and molecular dynamic (MD) simulations [41,43–47]. MC simulations are based on statistical mechanics [42] while MD simulations use atomic interaction potentials [43–47]. Both have the ability to capture ion transport and EDL formation at the electrode/electrolyte interface at the atomic scale [42–47]. However, MC and MD simulations cannot simulate long charging/

discharging processes with time scale similar to experimental cyclic voltammetry or galvanostatic cycling. In addition, they cannot simulate the multiscale nature of the processes taking place in actual EDLC devices with realistic electrode and electrolyte dimensions due to the excessively large number of atoms or molecules that it would require to simulate.

Finally, continuum models have been developed to investigate the charging/discharging dynamics of EDLCs with porous electrodes [48–59]. Continuum models can account for transport phenomena over the length scale of the electrode or the device and over the typical potential window and timescale of cyclic voltammetry or galvanostatic experiments. Most existing continuum models for EDLCs treat the electrode microarchitecture as homogeneous with some effective macroscopic properties determined from effective medium approximations (EMAs) based on porosity and specific area [48–59]. Unfortunately, these models cannot account for details of the 3D porous electrode architecture. On the other hand, Wang and Pilon [60] studied EDLC electrodes with 3D mesoporous structure but under equilibrium conditions. To the best of our knowledge, no continuum model simulations of 3D electrode architecture predicting the dynamic charging/discharging processes have been reported to date.

The objective of this study is to investigate the effect of electrode nanoarchitecture on the performance of EDLC porous electrodes consisting of highly-ordered monodisperse spherical carbon nanoparticles. To do so, cyclic voltammograms were numerically generated for different scan rates, electrode thicknesses, and carbon nanoparticle diameters arranged in simple cubic (SC) or face-centered cubic (FCC) packing. The numerical results were interpreted in light of normal electric field at the electrode/electrolyte interface, ion transport in the electrolyte, and resistive losses across the electrode.

3. Analysis

3.1. Schematic and assumptions

Fig. 1 shows schematics of the simulated EDLC electrodes consisting of (a) simple cubic (SC) or (b) face-centered cubic (FCC) packing of monodisperse carbon spheres of diameter d. By virtue of symmetry, a unit cell containing quarter-spheres was simulated. The current collector, electrode and electrolyte thicknesses were denoted by L_s, L_c, and L, respectively.

To make the problem mathematically tractable, the following assumptions were made: (1) The electrolyte was binary and symmetric, i.e., it consisted of two ion species of opposite valency $\pm z$ ($z > 0$). The two ion species were further assumed to have identical diameter a and diffusion coefficient D. (2) The Stern layer contained no free charge and its thickness H was approximated as the radius of the ions, so that $H = a/2$ [61,3,62]. (3) The transport properties of the electrodes and electrolyte were taken as constant except for the electrolyte dielectric constant $\varepsilon_r(E)$ which depended on the magnitude E of the local electric field vector. (4) Bulk motion of the electrolyte was negligible. (5) No redox reaction or ion intercalation took place within the electrode. (6) Heat generation was ignored and the EDLC was isothermal. (7) Electrical contact resistance between the carbon spheres was neglected.

3.2. Governing equations

The local electric potential $\psi(\mathbf{r}, t)$ in the electrode material was governed by the continuity equation combined with Ohm's law to yield [63,64]

$$\nabla \cdot (\sigma_c \nabla \psi) = 0 \tag{1}$$

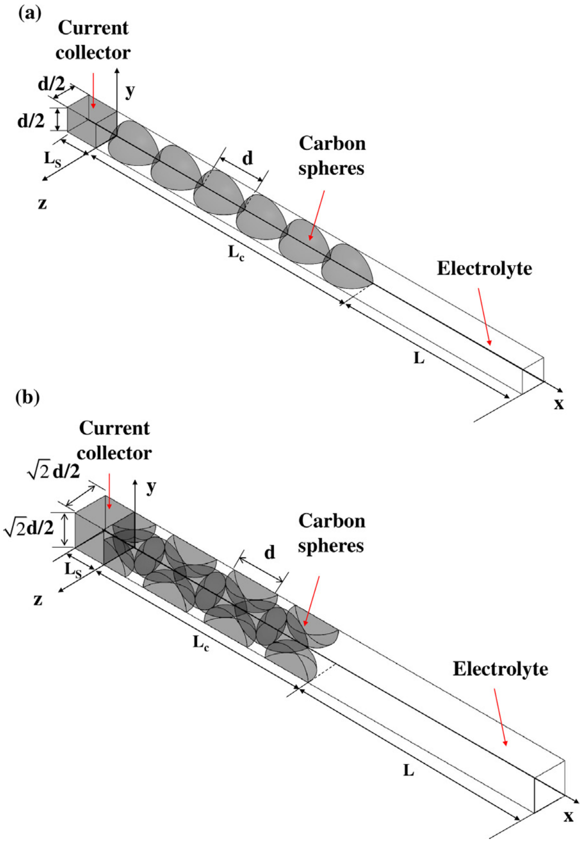

Fig. 1. Schematics of the EDLC electrodes simulated made of ordered carbon spheres of diameter d in (a) SC packing and (b) FCC packing.

where σ_c is the electrical conductivity of the electrode material (i.e., of the packed spheres).

The modified Poisson-Nernst-Planck (MPNP) model governed the spatiotemporal evolution of the electric potential $\psi(\mathbf{r}, t)$ and concentrations of the two ion species $c_i(\mathbf{r}, t)$ in the binary and symmetric electrolyte according to [65,66,37]

$$\nabla \cdot (\epsilon_0 \epsilon_r \nabla \psi) = \begin{cases} 0 & \text{in the Stern layer} \quad (2a) \\ -zF(c_1 - c_2) & \text{in the diffuse layer} \quad (2b) \end{cases}$$

with

$$\frac{\partial c_i}{\partial t} = -\nabla \cdot \mathbf{N}_i \qquad \textit{in the diffuse layer, for } i = 1, 2. \tag{2c}$$

Here, $\varepsilon_0 = 8.854 \times 10^{-12}$ F m^{-1} is the vacuum permittivity, ε_r is the field-dependent dielectric constant of the electrolyte, and $F = eN_A$ is the Faraday constant, with e and N_A being the elementary charge and Avogadro number, respectively. The mass flux vector $\mathbf{N}_i(\mathbf{r}, t)$ of ion species "i" (in mol/m^{2}s) at location $\mathbf{r}$ and time t was defined as [61]

$$\begin{aligned} \mathbf{N}_i(\mathbf{r}, t) = {} & -D\nabla c_i - \frac{zFDc_i}{R_u T}\nabla\psi \\ & - \frac{DN_A a^3 c_i}{1 - N_A a^3 (c_1 + c_2)} \nabla(c_1 + c_2), \textit{ for } i \\ & = 1, 2 \end{aligned} \tag{3}$$

where D is the diffusion coefficient of both ion species. The three terms on the right-hand side of Equation (3) correspond to the ion fluxes due to diffusion, electromigration, and steric effects, respectively [65,67]. This model accounts for finite ion size and is applicable to cases with large electric potential and/or electrolyte concentrations.

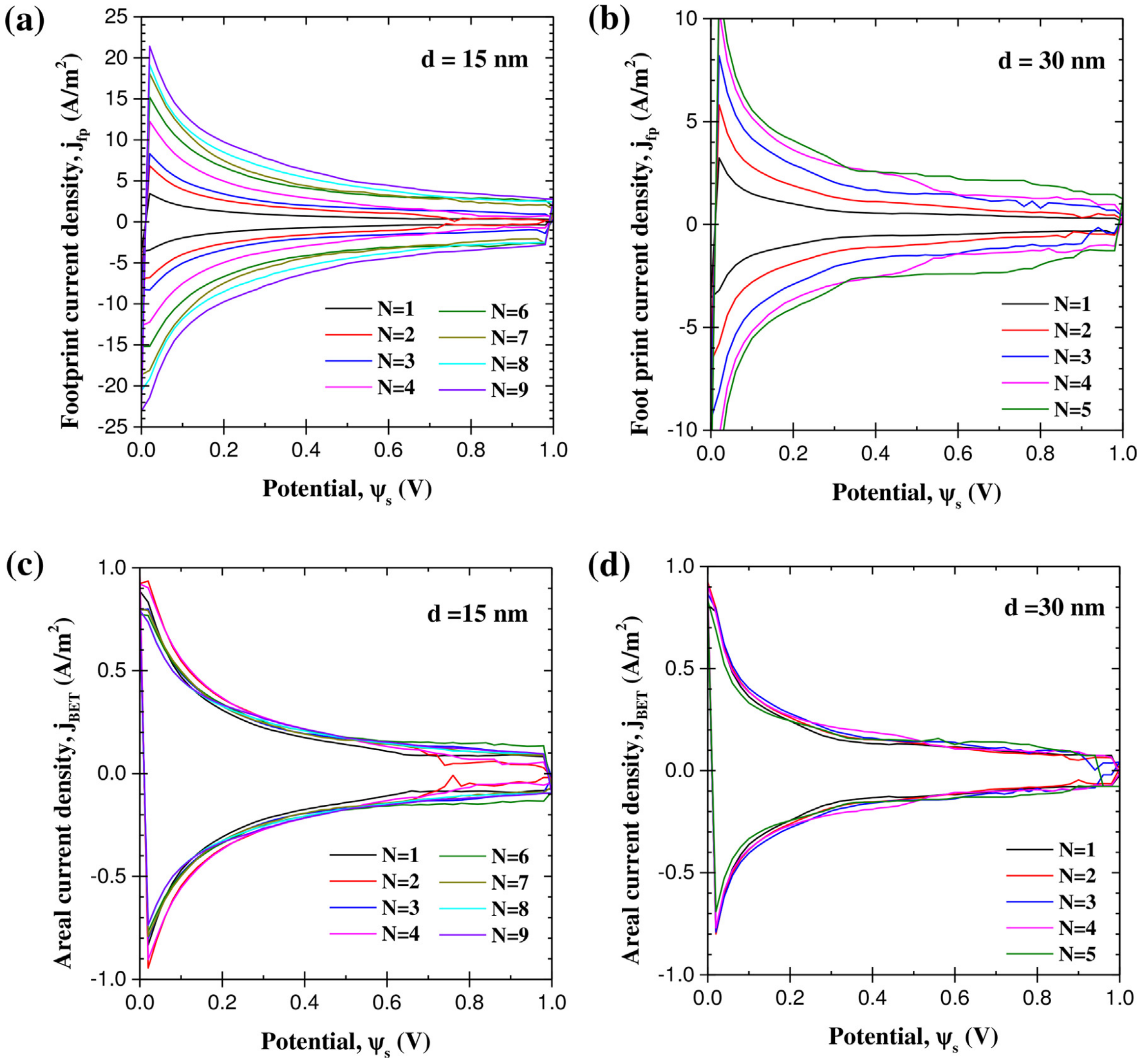

Fig. 2. (a, b) Footprint current density j_{fp} and (c, d) areal current density j_{BET} as functions of surface potential ψ_s at scan rate $\nu = 1$ V/s for carbon spheres in SC packing with diameter d of (a, c) $d = 15$ nm, and (b, d) $d = 30$ nm.

3.3. Initial and boundary conditions

In order to solve Equations (1) to (3) for the time-dependent potential $\psi(\mathbf{r}, t)$ and ion concentrations $c_i(\mathbf{r}, t)$ in the three-dimensional space, one needs one initial condition and two boundary conditions in each direction for each variable. Zero electric potential and uniform ion concentrations equal to the bulk concentrations c_∞ were used as initial conditions for solving the MPNP model, i.e.,

$$\psi(\mathbf{r},0) = 0\,\mathrm{V} \ \ and \ \ c_i(\mathbf{r},0) = c_\infty, \ for\ i = 1,2 \tag{4}$$

The potential at the current collector/electrode interface was imposed as $\psi_s(t)$. During cyclic voltammetry measurements, $\psi_s(t)$ varied linearly with time according to [61]

$$\psi_s(t) = \begin{cases} \psi_{\min} + v[t-(n_c-1)\tau_{CV}] & for\ (n_c-1)\tau_{CV} \le t < (n_c-1/2)\tau_{CV} \\ \psi_{\max} - v[t-(n_c-1/2)\tau_{CV}] & for\ (n_c-1/2)\tau_{CV} \le t < n_c\,\tau_{CV} \end{cases} \tag{5}$$

where n_c is the cycle number and τ_{CV} is the cycle period while ψ_{min} and ψ_{max} are the minimum and maximum values of the imposed potential $\psi_s(t)$, respectively. By virtue of symmetry in the two-electrode device, the boundary condition in the device centerline, located at $\mathbf{r}_{cl} = (x = L_c + L, y, z)$, was given by

$$\psi(\mathbf{r}_{cl}, t) = 0 \ \ and \ \ c_i(\mathbf{r}_{cl}, t) = c_\infty. \tag{6}$$

Moreover, the electric potential and current density were continuous across the spherical electrode/electrolyte interface located at $\mathbf{r}_{E/E}$ and planar current collector/electrolyte interface located at $\mathbf{r}_{C/E}$ so that

$$\psi(\mathbf{r}_k^-, t) = \psi(\mathbf{r}_k^+, t) \ \ and \ \ -\sigma_c \frac{\partial \psi}{\partial n}(\mathbf{r}_k^-, t) = -\varepsilon_0 \varepsilon_r \frac{\partial^2 \psi}{\partial n \partial t}(\mathbf{r}_k^+, t), \ with\ k = E/E\ or\ C/E \tag{7}$$

where $\partial/\partial n$ is the gradient normal to the electrode/electrolyte interface.

The electric potential varied linearly across the Stern layer [see Equation (2a)] so that the normal electric field at the planar and spherical Stern/diffuse layer interfaces, located at $\mathbf{r}_H$ satisfied [60,61]

$$\frac{\partial \psi}{\partial n}(\mathbf{r}_H, t) = \frac{\psi(\mathbf{r}_{C/E}) - \psi(\mathbf{r}_H)}{H}, \ for\ planar\ current\ collector\ surfaces, \tag{8}$$

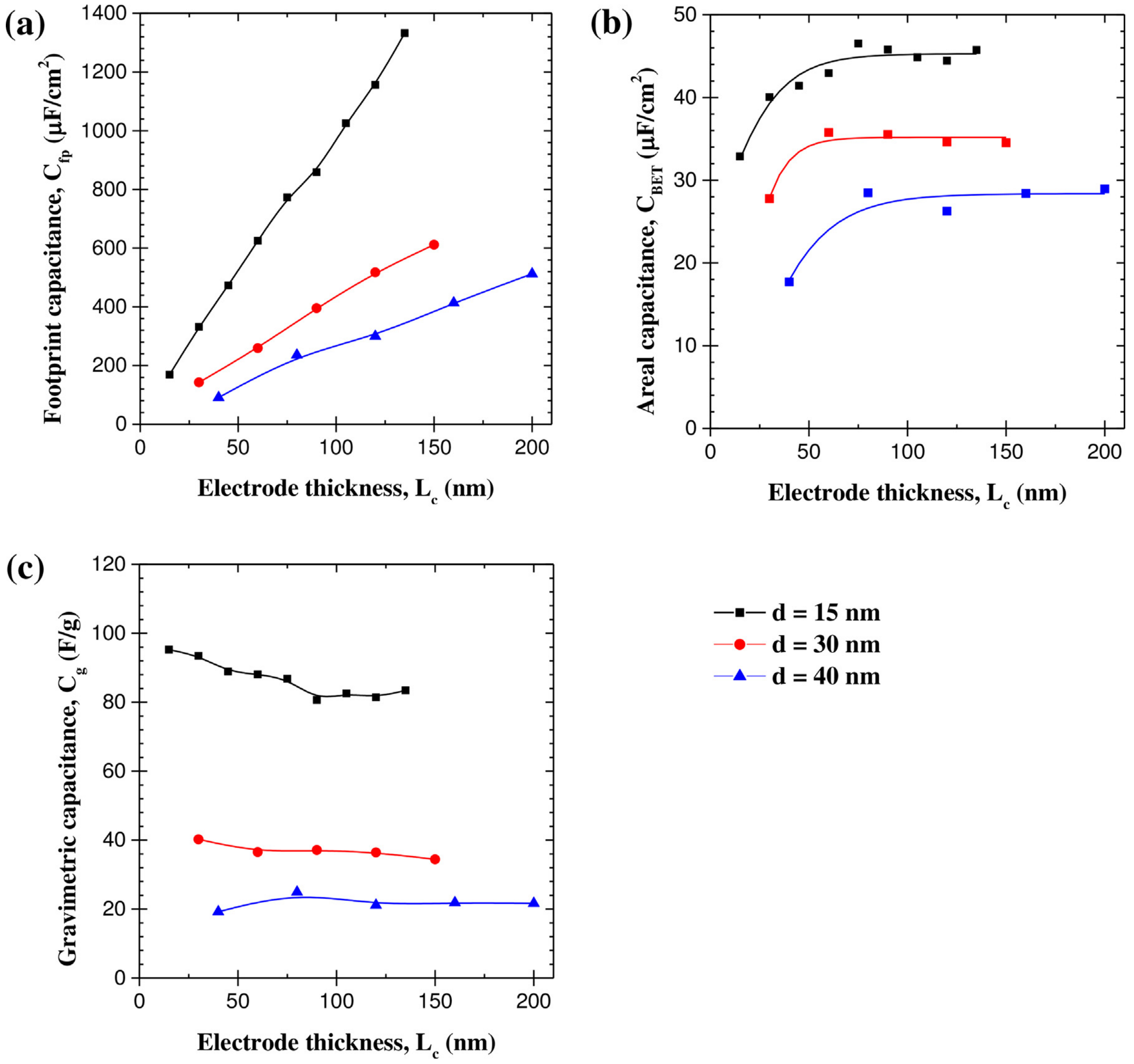

Fig. 3. (a) Footprint capacitance C_{fp}, (b) areal capacitance C_{BET}, and (c) gravimetric capacitance C_g as functions of electrode thickness L_c under quasi-equilibrium conditions (low scan rates) for carbon spheres in SC packing with diameter d = 15, 30, and 40 nm.

$$-\varepsilon_0\varepsilon_r\frac{\partial\psi}{\partial n}(\mathbf{r}_H,t) = C_s^{St}\frac{d}{d+2H})^2\left[\psi(\mathbf{r}_{E/E},t)-\psi(\mathbf{r}_H,t)\right],$$

for convex spherical electrode surfaces. (9)

Here, the Stern layer capacitance for a sphere of diameter d is given by the Helmholtz model expressed as [68]

$$C_s^{St} = \frac{\varepsilon_0\varepsilon_r}{H}(1+\frac{2H}{d}) \quad (10)$$

These boundary conditions accounted for the presence of the Stern layers without explicitly simulating them in the computational domain thus reducing significantly the number of meshes and making possible the numerical solution of the strongly coupled equations considered [60].

Based on assumption (5), no ion intercalated into the electrodes. Thus, the ion mass flux vectors vanished at the electrode/electrolyte and current collector/electrolyte interfaces such that [61]

$$\mathbf{N}_i(\mathbf{r}_k,t) = \mathbf{0} \quad \text{for } i = 1,2 \quad \text{with } k = E/E \text{ or } C/E. \quad (11)$$

By virtue of symmetry in the electrode packings, the normal electric field at the side walls of the simulated domain (Fig. 1) and the ion flux across the side walls also vanished, i.e., $\partial\psi/\partial n = 0$, and $\mathbf{N}_i = \mathbf{0}(i = 1, 2)$.

3.4. Constitutive relationships

In order to solve the transient 3D governing Equations (1) to (3) and their initial and boundary conditions, a total of 14 parameters were needed. These parameters include (i) the electrolyte properties ε_r, a, D, z, and c_∞, (ii) the electrode material conductivity σ_c, (iii) the electrode dimensions d, L_s, L_c, L, and (iv) the operating conditions ψ_{max}, ψ_{min}, T, and v.

The Booth model was used to account for the effect of the local electric field $\mathbf{E} = -\nabla\psi$ on the electrolyte dielectric constant expressed as [60,69–72],

$$\epsilon_r(E) = \begin{cases} n^2 + (\epsilon_r(0) - n^2)\dfrac{3}{\beta E}\left[\coth(\beta E) - \dfrac{1}{\beta E}\right] & \text{for } E \geq 10^7 \text{ V/m} \quad (12) \\ \epsilon_r(0) & \text{for } E < 10^7 \text{ V/m} \quad (13) \end{cases}$$

where n is the refractive index of the electrolyte solution, $\varepsilon_r(0)$ is the dielectric constant at zero electric field, and β is a semi-empirical constant. The electrolyte simulated was $(C_2H_5)_4NBF_4$

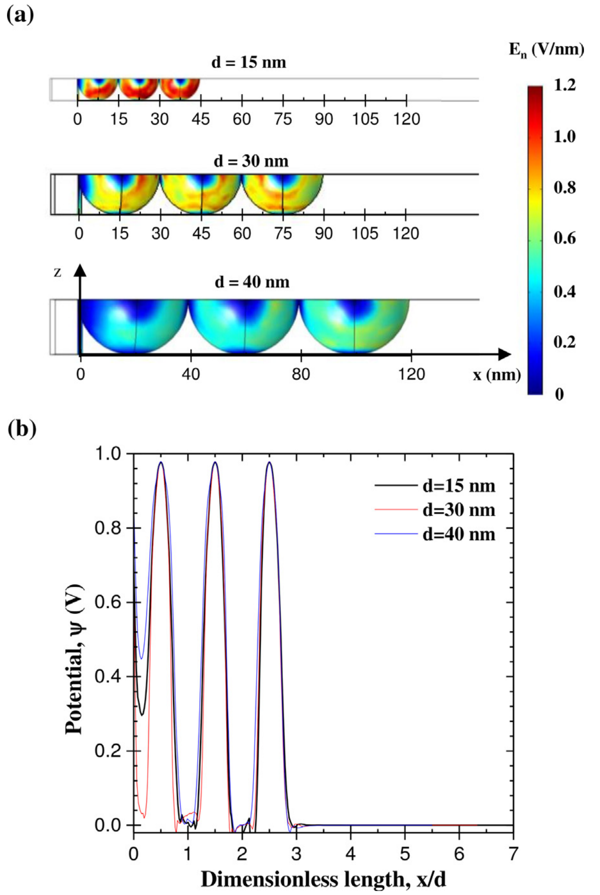

Fig. 4. (a) Magnitude of the normal electric field E_n at the surface of carbon spheres for electrodes made of 3 carbon spheres in SC packing with diameter $d = 15$, 30, or 40 nm at $t = 0.49\tau_{CV}$ (or $\psi_s = 0.98$ V). (b) Corresponding electric potential $\psi(x/d)$ as a function of x/d along the x-direction given by ($0 \le x \le L$, $y = 0$, $z = d/2$).

(TEABF$_4$) in propylene carbonate at room temperature featuring n = 1.42 [73], $\varepsilon_r(0)$ = 64.4 [74], and β = 1.314 x 10 $^{-8}$ m/V [69]. In addition, the bare ion diameter a of (C$_2$H$_5$)$_4$N$^+$ and BF$_4^-$ were 0.68 nm and 0.33 nm [75]. However, as discussed in Refs. [76,65], “Smaller bare ions tend to be more heavily solvated and therefore have larger effective diameters”. Moreover, electrolyte ions are less solvated when the electrolyte concentration increases, resulting in smaller effective ion diameter [11,77–80]. Considering the fact that the solubility of (C$_2$H$_5$)$_4$NBF$_4$ in propylene carbonate at room temperature is 1 mol/L [81], the effective ion diameters of (C$_2$H$_5$)$_4$N$^+$ and BF$_4^-$ were assumed to be identical and equal to 0.68 nm. Furthermore, the diffusion coefficient D of (C$_2$H$_5$)$_4$N$^+$ ions and BF$_4^-$ in propylene carbonate at room temperature was taken as 3.17 x 10^{-10} m^2/s [82]. The ion valency was $z = 1$ and bulk concentration of the ion species was chosen as $c_\infty = 1$ mol/L, as commonly used experimentally [27]. In addition, the value was chosen as $\sigma_c = 5$ S/m based on the typical range of conductivity of carbon between 10^{-6} and 10^2 S/m [83,84]. Moreover, the thickness of the planar current collector was taken as $L_s = 10$ nm and the length of the electrolyte domain simulated was $L = 100$ nm. The thickness of the porous carbon electrode L_c as well as the diameter of the carbon spheres d were treated as variables. Finally, the temperature was taken as room temperature, i.e. $T = 298$ K. The electrode was cycled between ψ_{min} = 0 V and ψ_{max} = 1 V. The scan rate varied from 1 to 10^5 V/s.

3.5. Method of solution

The governing equations along with the initial and boundary conditions were solved using COMSOL 4.4. Mesh element size was chosen to be the smallest at the electrode/electrolyte interface where ion concentration gradient and potential gradient were the largest. Moreover, the numerical convergence was considered to be reached when the local electric potential $\psi(\mathbf{r}, t)$ and the normal current density $j_n = \mathbf{j} \cdot \mathbf{n}$ at the electrode/electrolyte interface changed within 1% when reducing the minimum mesh element size and mesh growth rate in the boundary layer near the electrode/electrolyte interfaces by a factor of two. For example, the total number of finite elements was on the order of 10^7 for the simulations of electrodes made of 5 ordered carbon spheres shown in Fig. 1. In addition, the adaptive time step was controlled by the relative and absolute tolerance set to be 0.01 and 0.001. This enabled the use of smaller time step when potential and current density changed more rapidly. The simulations were run on Hoffman2 shared computing cluster of UCLA with 8 to 12 processors and 32 to 64 GB of RAM.

Finally, several cycles were simulated and an oscillatory steady state in $\psi(\mathbf{r}, t)$ and $j_n = \mathbf{j} \cdot \mathbf{n}$ was considered to be reached when the maximum relative error between the value of each variable at time t and its value at time t$-\tau_{CV}$ throughout the computational domain was less than 1%. These conditions were typically met by the third cycle for all conditions simulated. The CPU time for each simulation reported ranged between 1 and 4 days.

3.6. Data processing

Cyclic voltammetry simulations consist of imposing a triangular time-dependent potential $\psi_s(t)$ [Equation (5)] and predicting the current density to plot CV curves. The current density at the electrode/electrolyte and current collector/electrolyte interfaces arising from the formation and dissolution of electric double layer was expressed (in A/m^2) as [61,85]

$$j_n(\mathbf{r}_k, t) = -\varepsilon_0 \varepsilon_r \frac{\partial}{\partial t} \frac{\partial \psi}{\partial n}(\mathbf{r}_k, t), \ \textit{with}\ k = E/E\ \textit{or}\ C/E. \tag{14}$$

The current densities averaged over the footprint area, electrode/electrolyte interface area, and mass of the electrode respectively denoted by j_{fp} (in A/m^2), j_{BET} (in A/m^2), and j_g (in A/g) can be defined as

$$j_{fp}(t) = \frac{\iint_{A_{BET}} j_n(\mathbf{r}, t) dA_{BET}}{A_{fp}}, \ j_{BET}(t) = \frac{\iint_{A_{BET}} j_n(\mathbf{r}, t) dA_{BET}}{A_{BET}}, \ j_g(t) = \frac{\iint_{A_{BET}} j_n(\mathbf{r}, t) dA_{BET}}{m} \tag{15}$$

where A_{fp} is the footprint area of the electrode, corresponding to the area of the planar current collector, A_{BET} is the electrode/electrolyte interfacial area that can be measured experimentally by the Brunauer-Emmett-Teller (BET) method, and m is the total mass of all the carbon spheres constituting the electrode.

The corresponding capacitances can be estimated from the predicted CV curves according to [86]

$$C_k(v) = \frac{1}{\psi_{\max} - \psi_{\min}} \oint \frac{j_k(t)}{2v} d\psi_s, \ \textit{with}\ k = fp,\ BET,\ \textit{or}\ g. \tag{16}$$

where $j_k(t)$ is given by Equation (15), v is the scan rate, and ψ_s is the potential imposed at the current collector and given by Equation (5).

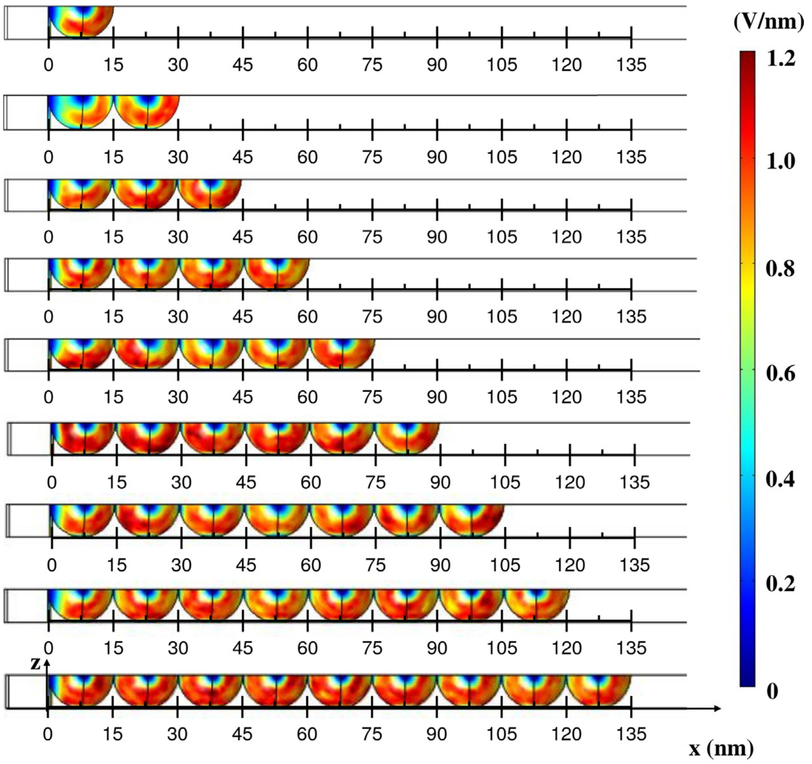

Fig. 5. Magnitude of the normal electric field E_n at the surface of carbon spheres for electrodes made of 1 to 9 carbon spheres in SC packing with diameter $d = 15$ nm at $t = 0.49\tau_{CV}$ (or $\psi_s = 0.98$ V).

4. Results and discussion

4.1. Influence of carbon sphere number and diameter

CV curves of electrodes made of carbon spheres in SC packing were simulated under quasi-equilibrium conditions corresponding to situations when the capacitance was independent of scan rate [61]. Figures 2(a) and 2 (b) show the footprint current density j_{fp} as a function of the imposed potential ψ_s, at scan rate $v = 1$ V/s, for electrodes made of N carbon spheres in SC packing with diameter d equals to either 15 nm ($1 \leq N \leq 9$) or 30 nm ($1 \leq N \leq 5$), corresponding to BET surface area of 200 m^2/g and 100 m^2/g, respectively. These figures indicate that for given sphere diameter and surface potential, the footprint current density increased with increasing sphere number. This can be attributed to the increasing electrode surface area with increasing carbon sphere number N while the footprint remained unchanged. In fact, Figures 2(c) and 2 (d) plot the current density j_{BET} per unit surface area of electrode/electrolyte interface as a function of imposed potential ψ_s for d equals to 15 and 30 nm, respectively. These figures establish that the areal current density j_{BET} was weakly dependent of the number N of carbon spheres. In other words, the total current i (in A) was linearly proportional to the BET surface area A_{BET}.

Moreover, Fig. 3 shows (a) the footprint capacitance C_{fp}, (b) the areal capacitance C_{BET}, and (c) the gravimetric capacitance C_g of electrodes made of multiple carbon spheres in SC packing with diameter d of 15, 30, and 40 nm as functions of the electrode thickness $L_c (= Nd)$ under quasi-equilibrium conditions. It indicates that all three capacitances C_{fp}, C_{BET}, and C_g decreased with increasing sphere diameter d for a given electrode thickness L_c. On the other hand, for a given sphere diameter d, C_{fp} increased almost linearly with increasing electrode thickness L_c. On the other hand, C_{BET} first increased with increasing electrode thickness L_c then reached a plateau for $L_c \geq 75$ nm. Finally, Cg remained nearly constant for all electrode thicknesses considered. Note that the capacitance C_{BET} ranged between 10 and 50 $\mu F/cm^2$ while C_g ranged between 20 and 100 F/g. These values were comparable with reported experimental measurements for electrodes with similar nanoarchitecture [12,11,22]. For example, areal capacitance C_{BET} was reported to be between 10 and 15 $\mu F/cm^2$ [11] and C_g between 60 and 110 F/g [12,11] for electrodes made of ordered mesoporous carbon spheres in non-aqueous electrolytes under cyclic voltammetry with potential window of 3 V [11] or 2 V [12]. In addition, Kim et al. [22] reported gravimetric capacitance C_g around 60 F/g for carbon electrodes with similar nanoarchitecture and potential windows in aqueous electrolytes under galvanostatic cycling with small current. To explain the trends in C_{fp}, C_{BET}, and C_g

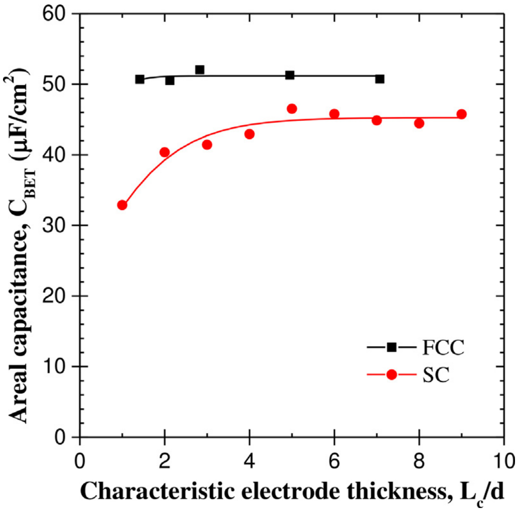

Fig. 6. Areal capacitance C_{BET} as a function of the dimensionless electrode thickness L_c/d under quasi-equilibrium conditions (low scan rates) for carbon spheres in either FCC or SC packing with diameter $d = 15$ nm.

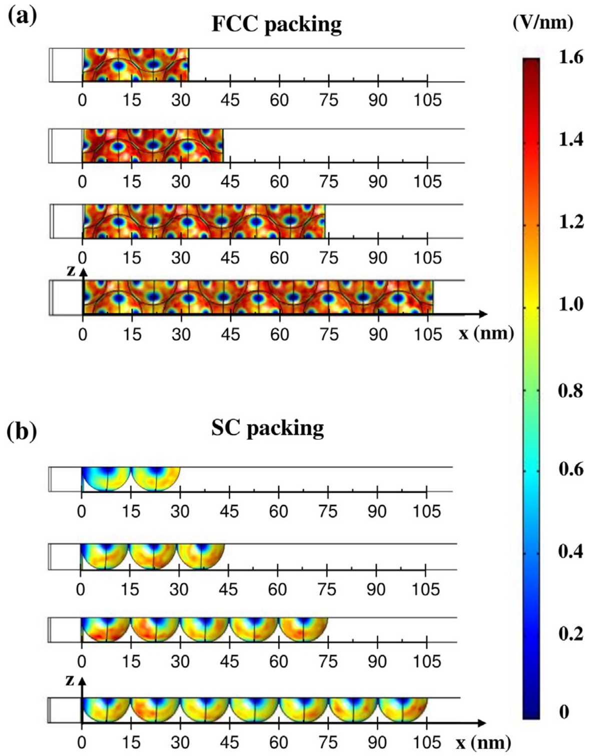

Fig. 7. Magnitude of the normal electric field E_n at the surface of carbon spheres in (a) FCC packing and (b) SC packing with diameter $d = 15$ nm at $t = 0.98\tau_{CV}$ (or $\psi_s = 0.98$ V).

as functions of sphere diameter d and electrode thickness L_c, one needs to consider the normal electric field at the sphere surfaces.

Fig. 4(a) shows the magnitude of the normal component E_n of the local electric field (i.e., $E_n = \mathbf{E} \cdot \mathbf{n} = -\partial\psi/\partial n$) at the electrode/electrolyte interface for $N = 3$ spheres in SC packing with diameter d of 15, 30, and 40 nm, at $t = 0.49\tau_{CV}$ corresponding to $\psi_s = 0.98$ V, i.e., near the end of the charging stage. Note that, during charging, the normal electric field increased everywhere at the electrode surface but the relative profile remained unchanged. Fig. 4(a) indicates that the magnitude of the normal electric field E_n increased with decreasing sphere diameter d. This can be attributed to the fact that for smaller spheres, the electric potential decayed from $\psi(\mathbf{r}_{E/E}, t) \approx \psi_s(t)$ at the electrode surface to zero in the local bulk electrolyte within the porous electrode structure over a smaller distance. To further illustrate the effect of sphere diameter on the normal electric field, Fig. 4(b) plots the electric potential along the x-direction as a function of the dimensionless position x/d at $t = 0.49\tau_{CV}$ for sphere diameter d equals to 15, 30, and 40 nm. It indicates that the electric potential profile scaled with x/d. In other words, the potential $\psi(x/d)$ and its derivative $\partial\psi/\partial(x/d)$ were independent of d, as were $\partial\psi/\partial(y/d)$ and $\partial\psi/\partial(z/d)$ (not shown). Therefore, the magnitude of the normal electric field $-\partial\psi/\partial n$ at the electrode surface was proportional to $1/d$. Thus, for a given potential, electrodes consisting of smaller carbon spheres attracted more ions to their surface resulting in larger areal or gravimetric charge densities (see Figure S1 in supplementary material). Consequently, the capacitances C_{fp}, C_{BET}, and C_g increased with decreasing sphere diameter d [Fig. 3(a)].

Fig. 5 shows the magnitude of the normal electric field E_n for electrodes made of 1 to 9 carbon spheres in SC packing for diameter d of 15 nm at $t = 0.49\tau_{CV}$. The systematically smaller value of E_n resulted in less charge storage on the surface of the first sphere facing the planar current collector (see Figure S2 in supplementary material). This was due to the fact that the planar current collector and the first sphere were at nearly the same potential $\psi_s(t)$ at all times t. On the other hand, the magnitude of the normal electric field E_n on other spheres remained unchanged with increasing sphere number N. Thus, the initial rise and the plateau in C_{BET} with increasing electrode thickness L_c or sphere number N [Fig. 3(b)] can be attributed to the decreasing relative contribution of the first sphere to the total charge storage.

4.2. Influence of electrode morphology

Fig. 6 shows the areal capacitance C_{BET} as a function of the dimensionless electrode thickness L_c/d for the electrodes made of carbon spheres in either SC or FCC packings with diameter d of 15 nm under quasi-equilibrium conditions, i.e., low scan rate. It indicates that C_{BET} increased with increasing thickness for SC packing before reaching a plateau for $L_c/d \geq 5$. By contrast, C_{BET} for electrodes with FCC packing was independent of electrode thickness. Moreover, Fig. 6 establishes that for any given electrode thickness, the areal capacitance of electrodes made of carbon spheres in FCC packing was systematically larger than that in SC packing.

Fig. 7 compares the magnitude of the normal electric field at the electrode/electrolyte interface for electrodes made of multiple carbon spheres in SC and FCC packings for diameter d of 15 nm, at $t = 0.49\tau_{CV}$ corresponding to $\psi_s = 0.98$ V. It indicates that for similar electrode thickness L_c, the magnitude of the normal electric field E_n at the carbon sphere surface was larger for FCC packing structure than for SC packing, resulting in larger capacitance C_{BET} (Fig. 6). This can be attributed to the fact that the FCC structure was denser and featured less distance for the electric potential to decay from $\psi(\mathbf{r}_{E/E}, t) \approx \psi_s(t)$ at the carbon sphere surfaces to zero in the local bulk electrolyte within the porous electrode structure.

Fig. 8(a) shows the areal capacitance C_{BET} for the electrodes made of carbon spheres in FCC packing with 3 ($L_c = 2.12d$) and 10 ($L_c = 7.07d$) rows of spheres and in SC packing with 2 ($L_c = 2d$) and 7 ($L_c = 7d$) spheres as a function of scan rate v. It indicates that C_{BET} was independent of scan rate (quasi-equilibrium regime) for both FCC and SC packings at low scan rates. In addition, the electrodes made of carbon spheres in FCC packing had larger capacitance than that with SC packing, as previously observed (Fig. 6). However, regardless of carbon sphere packing structure (SC or FCC), the capacitance C_{BET} dropped sharply at a critical scan rate which decreased with increasing electrode thickness. This could be due to ion diffusion limitation in the tortuous electrode structure and/or resistive losses in the potential propagation across the electrode at high scan rates.

Fig. 8(b) shows the areal capacitance C_{BET} as a function of scan rate v for the electrodes made of 2 carbon spheres in SC packing with ion diffusion coefficient D equals to 3.17×10^{-9}, 3.317×10^{-10}, and 3.17×10^{-11} m^2/s. It indicates that the diffusion coefficient had no effect on the capacitance at any scan rate considered. In other words, the decrease in capacitance at high scan rates was not due to ion diffusion limitation through the porous electrode. On the other hand, Fig. 8(c) shows the areal capacitance C_{BET} as a function of scan rate v for electrodes made of 2 spheres with diameter $d = 15$ nm in SC packing and electrical conductivity σ_c of 5, 0.5, and 0.05 S/m. It indicates that the sharp drop in C_{BET} occurred at smaller critical scan rate as the electrical conductivity σ_c decreased. In fact, the potential propagation across the electrode was limiting the capacitance C_{BET} at high scan rates. Note that Wang and Pilon [85] previously observed ion diffusion limitation for planar (i.e., nonporous) electrodes resulting in the sharp drop in C_{BET} at high scan rates. However, the sharp drop in C_{BET} was observed at higher scan rate than in the present study. In the porous electrodes under

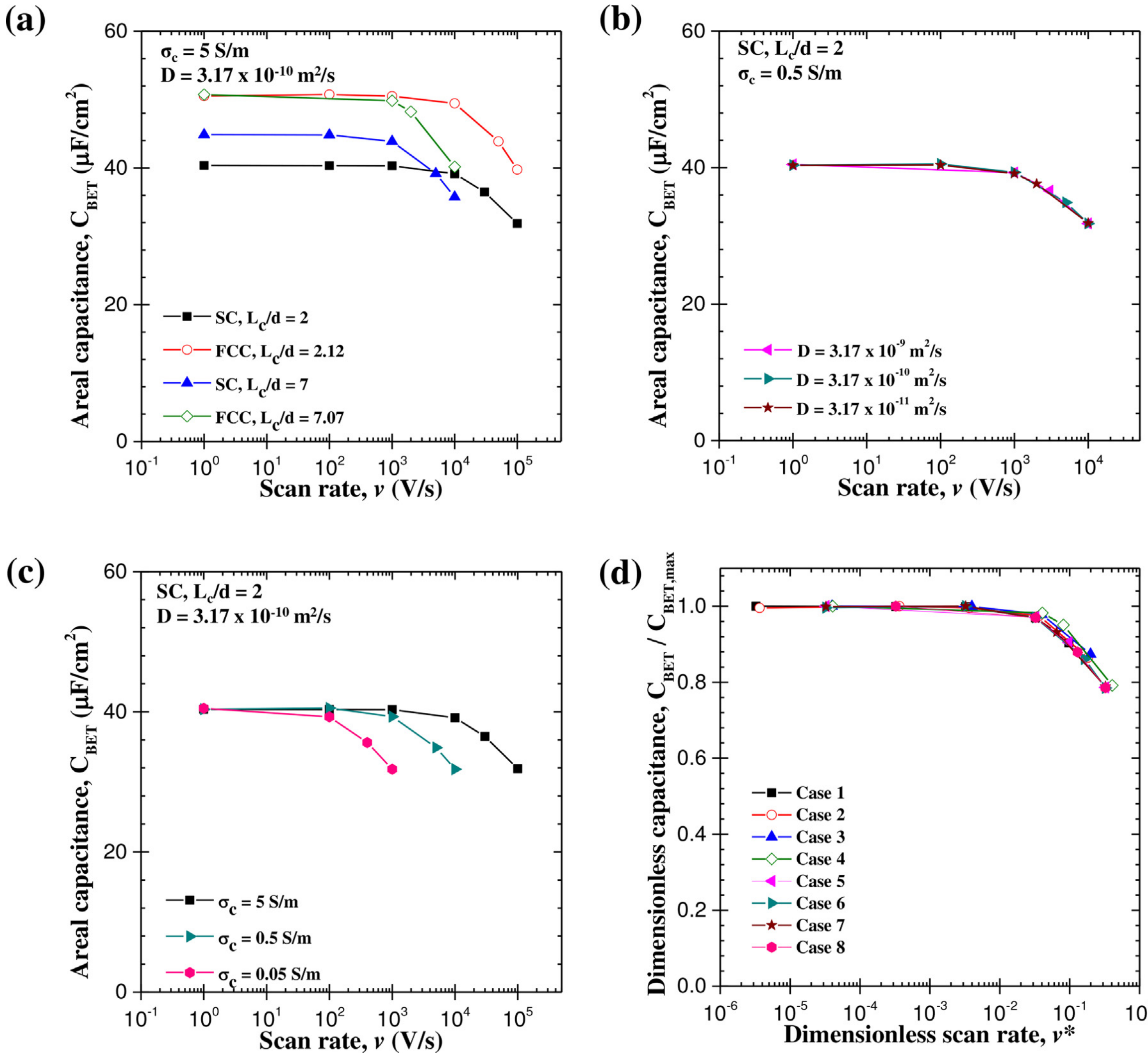

Fig. 8. (a) Areal capacitance C_{BET} of electrodes made of FCC and SC packing of carbon spheres with diameter d = 15 nm as functions of scan rate v for different (a) electrode thicknesses, (b) diffusion coefficients, and (c) electrode conductivities. (b) Dimensionless areal capacitance $C_{BET}/C_{BET,max}$ of electrodes made of FCC and SC packing of carbon spheres with diameter d = 15 nm as functions of dimensionless scan rate v^* with parameters L_c/d, D, σ_c and morphology summarized in Table 1.

consideration, resistive losses limited capacitance before ion diffusion at high scan rates.

Finally, Fig. 8(d) shows the dimensionless capacitance $C_{BET}/C_{BET,max}$ as a function of dimensionless scan rate v^* for both FCC and SC packings with diameter d = 15 nm and for different values of electrical conductivity σ_c, ion diffusion coefficient D, and electrode thickness L_c, as summarized in Table 1.

In addition, the dimensionless scan rate v^* was expressed as [85]

$$v^* = \frac{v\tau_e}{\psi_{\max} - \psi_{\min}} = \frac{\tau_e}{\tau_{CV}/2} \tag{17}$$

where τ_{CV} is the CV cycle period and the time scale τ_e is chosen to be the characteristic time for potential propagation (i.e., for electron transport in the electrode material) instead of the diffusion time scale $\tau_D = L^2/D$ used by Wang and Pilon [85]. This time scale τ_e can be expressed as [87]

$$\tau_e = \frac{L_c}{u_e} = \frac{\rho_c n_e e L_c^2}{M_c(\psi_{\max} - \psi_{\min})\sigma_c}. \tag{18}$$

Here, L_c is the thickness of the porous carbon electrode, u_e is the so-called drift velocity, i.e., the average velocity of electrons under electric field $E = (\psi_{max} - \psi_{min})/L_c$, and expressed as $u_e = (M_c\sigma_c E)/(\rho_c n_e e)$, where ρ_c is the density of the electrode material, n_e is the number of free electrons per atom in the electrode material, M_c is the atomic mass (in u) of the electrode material and σ_c is the electrode material electrical conductivity. For carbon nanospheres, ρ_c = 500 kg/m^3 [84], n_e = 1, and M_c = 12.01 u. Fig. 8(d) indicates that the capacitance ratio $C_{BET}/C_{BET,max}$ for electrodes with different electrical conductivity σ_c, ion diffusion coefficient D, electrode thickness L_c, and packing structures collapsed on the same curve when plotted as a function of dimensionless scan rate v^*. In addition, for dimensionless scan rate v^* smaller than 0.3, the areal capacitance was maximum and rate-independent, corresponding

Table 1
Parameters for eight cases of dimensionless capacitances reported in Fig. 8(d)

Case number	L_c/d	Morphology	D (m²/s)	σ_c (S/m)
1	2	SC	3.17 x 10^{-10}	5
2	2.12	FCC	3.17 x 10^{-10}	5
3	7	SC	3.17 x 10^{-10}	5
4	7.07	FCC	3.17 x 10^{-10}	5
5	2	SC	3.17 x 10^{-9}	0.5
6	2	SC	3.17 x 10^{-10}	0.5
7	2	SC	3.17 x 10^{-11}	0.5
8	2	SC	3.17 x 10^{-10}	0.05

to $v \le \alpha/[(\psi_{\max} - \psi_{\min})^2 L_c^2]$ where $\alpha = 0.3 M_c \sigma_c / \rho_c n_e e$ depends only on the electrode material. Thus, electrode materials with large values of α are desirable to achieve high rate performance. For example, $\alpha = 4.7$ for gold [88] while α ranges between $7.5 \text{ x } 10^{-8} - 1.2 \text{ x } 10^{-3}$ for carbon nanoparticles [84] and between $4.1 \text{ x } 10^{-13} - 1.5 \text{ x } 10^{-4}$ for activated carbon (porous) [83,84] depending on their electrical conductivity and density.

5. Conclusion

This paper presented, for the first time, three-dimensional transient simulations of EDLC electrodes consisting of monodisperse carbon spheres with different diameters and ordered in FCC and SC packing structures under cyclic voltammetry. Simulations were based on a continuum model accounting for interfacial and transport phenomena throughout the electrode and the electrolyte. For any given morphology, the areal capacitance increased with decreasing sphere diameter. In addition, FCC packing featured larger capacitance than SC packing. These results were explained by considering the magnitude of the electric field at the carbon spheres/electrolyte interfaces. Moreover, for all cases considered, the areal capacitance remained constant at low scan rate but decreased beyond a critical scan rate when potential propagation across the electrode could not follow the rapid changes in the potential imposed at the current collector. In fact, the rate-dependent regime of capacitance was reached at lower scan rates for thicker electrodes, regardless of the electrode morphology. Finally, dimensional analysis was performed to collapse capacitance versus scan rate plots, based on ratio of CV cycle period and the time scale for electron transport in the electrode. These results and the computational tools developed can be used to design and optimize EDLC electrodes to maximize their capacitance and energy and/or power densities.

Acknowledgment

The computation for this study was performed on the Hoffman2 cluster hosted by the Academic Technology Services (ATS) at the University of California, Los Angeles, USA. In addition, this material is based upon work supported, in part, by the China Scholarship Council (CSC).

Appendix A. Supplementary Data

Supplementary data associated with this article can be found, in the online version, at http://dx.doi.org/10.1016/j.electacta.2017.09.060.

References

[1] B.E. Conway, Electrochemical Supercapacitors: Scientific Fundamentals and Technological Applications, Kluwer Academic/Plenum Publishers, New York, NY, 1999.

[2] US Department of Energy, Basic Research Needs for Electrical Energy Storage: Report of the Basic Energy Sciences Workshop for Electrical Energy Storage, Tech. Rep., Office of Basic Energy Sciences, DOE, 2007.

[3] A.J. Bard, L.R. Faulkner, J. Leddy, C.G. Zoski, Electrochemical Methods: Fundamentals and Applications, vol. 2, John Wiley & Sons, Hoboken, NJ, 1980.

[4] V.S. Bagotsky, Fundamentals of Electrochemistry, 2nd edition, John Wiley & Sons, Hoboken, NJ, 2006.

[5] L.L. Zhang, Y. Gu, X. Zhao, Advanced porous carbon electrodes for electrochemical capacitors, Journal of Materials Chemistry A 1 (33) (2013) 9395–9408.

[6] H.E.Z. Abidin, A.A. Hamzah, B.Y. Majlis, Electrical characterization of Interdigital Electrode based on cyclic voltammetry performances, in Semiconductor Electronics (ICSE), 2012 10th IEEE International Conference on. IEEE, 2012, pp. 348–351.

[7] F. Stoeckli, T.A. Centeno, Optimization of the characterization of porous carbons for supercapacitors, Journal of Materials Chemistry A 1 (23) (2013) 6865–6873.

[8] J. Zhi, Y. Wang, S. Deng, A. Hu, Study on the relation between pore size and supercapacitance in mesoporous carbon electrodes with silica-supported carbon nanomembranes, RSC Advances 4 (76) (2014) 40296–40300.

[9] L. Mao, Y. Zhang, Y. Hu, K.H. Ho, Q. Ke, H. Liu, Z. Hu, D. Zhao, J. Wang, Activation of sucrose-derived carbon spheres for high-performance supercapacitor electrodes, RSC Advances 5 (12) (2015) 9307–9313.

[10] V.R. Gonçales, M.P. Massafera, T.M. Benedetti, D.G. Moore, S.I. Torresi, R.M. Torresi, Nanostructured thin films obtained by electrodeposition over a colloidal crystal template: applications in electrochemical devices, Journal of the Brazilian Chemical Society 20 (4) (2009) 663–673.

[11] H.-J. Liu, W.-J. Cui, L.-H. Jin, C.-X. Wang, Y.-Y. Xia, Preparation of three-dimensional ordered mesoporous carbon sphere arrays by a two-step templating route and their application for supercapacitors, Journal of Materials Chemistry 19 (22) (2009) 3661–3667.

[12] C. Vix-Guterl, S. Saadallah, K. Jurewicz, E. Frackowiak, M. Reda, J. Parmentier, J. Patarin, F. Béguin, Supercapacitor electrodes from new ordered porous carbon materials obtained by a templating procedure, Materials Science and Engineering B 108 (1-2) (2004) 148–155.

[13] H.-Q. Li, R.-L. Liu, D.-Y. Zhao, Y.-Y. Xia, Electrochemical properties of an ordered mesoporous carbon prepared by direct tri-constituent co-assembly, Carbon 45 (13) (2007) 2628–2635.

[14] M. Endo, T. Maeda, T. Takeda, Y.J. Kim, K. Koshiba, H. Hara, M.S. Dresselhaus, Capacitance and pore-size distribution in aqueous and nonaqueous electrolytes using various activated carbon electrodes, Journal of The Electrochemical Society 148 (8) (2001) 910–914.

[15] A.B. Fuertes, G. Lota, T.A. Centeno, E. Frackowiak, Templated mesoporous carbons for supercapacitor application, Electrochimica Acta 50 (14) (2005) 2799–2805.

[16] W. Xing, S.Z. Qiao, R.G. Ding, F. Lid, G.Q. Lu, Z.F. Yan, H.M. Cheng, Superior electric double layer capacitors using ordered mesoporous carbons, Carbon 44 (2) (2006) 216–224.

[17] C. Portet, G. Yushin, Y. Gogotsi, Effect of carbon particle size on electrochemical performance of edlc, Journal of The Electrochemical Society 155 (7) (2008) A531–A536.

[18] R. Lin, P.L. Taberna, J. Chmiola, D. Guay, Y. Gogotsi, P. Simon, Microelectrode study of pore size ion size and solvent effects on the charge/discharge behavior of microporous carbons for electrical double-layer capacitors, Journal of The Electrochemical Society 156 (1) (2009) 7–12.

[19] F. Li, N. van der Laak, S.-W. Ting, K.-Y. Chan, Varying carbon structures templated from kit-6 for optimum electrochemical capacitance, Electrochimica Acta 55 (8) (2010) 2817–2823.

[20] P. Simon, Y. Gogotsi, Materials for electrochemical capacitors, Nature Materials 7 (11) (2008) 845–854.

[21] E. Frackowiak, Carbon materials for supercapacitor application, Physical Chemistry Chemical Physics 9 (15) (2007) 1774–1785.

[22] S.-K. Kim, E. Jung, M.D. Goodman, K.S. Schweizer, N. Tatsuda, K. Yano, P.V. Braun, Self-assembly of monodisperse starburst carbon spheres into hierarchically organized nanostructured supercapacitor electrodes, ACS Applied Materials & Interfaces 7 (17) (2015) 9128–9133.

[23] D.-D. Zhou, H.-J. Liu, Y.-G. Wang, C.-X. Wang, Y.-Y. Xia, Ordered mesoporous/microporous carbon sphere arrays derived from chlorination of mesoporous TiC/C composite and their application for supercapacitors, Journal of Materials Chemistry 22 (5) (2012) 1937–1943.

[24] H. Zhou, S. Zhu, M. Hibino, I. Honma, Electrochemical capacitance of self-ordered mesoporous carbon, Journal of Power Sources 122 (2) (2003) 219–223.

[25] D.W. Wang, F. Li, H.T. Fang, M. Liu, G.Q. Lu, H.M. Cheng, Effect of pore packing defects in 2-D ordered mesoporous carbons on ionic transport, Journal of Physical Chemistry B 110 (17) (2006) 8570–8575.

[26] H. Yamada, H. Nakamur, F. Nakahara, I. Moriguchi, T. Kudo, Electrochemical study of high electrochemical double layer capacitance of ordered porous carbons with both meso/macropores and micropores, Journal of Physical Chemistry C 111 (1) (2007) 227–233.

[27] S.W. Woo, K. Dokko, H. Nakano, K. Kanamura, Preparation of three dimensionally ordered macroporous carbon with mesoporous walls for electric double-layer capacitors, Journal of Materials Chemistry 18 (14) (2008) 1674–1680.

[28] H.J. Liu, X.M. Wang, W.J. Cui, Y.Q. Dou, D.Y. Zhao, Y.Y. Xia, Highly ordered mesoporous carbon nanofiber arrays from a crab shell biological template and its application in supercapacitors and fuel cells, Journal of Materials Chemistry 20 (20) (2010) 4223–4230.

[29] G. Sun, J. Wang, X. Liu, D. Long, W. Qiao, L. Ling, Ion transport behavior in triblock copolymer-templated ordered mesoporous carbons with different pore symmetries, Journal of Physical Chemistry C 114 (43) (2010) 18745–18751.

[30] B.E. Conway, W.G. Pell, Power limitations of supercapacitor operation associated with resistance and capacitance distribution in porous electrode devices, Journal of Power Sources 105 (2) (2002) 169–181.

[31] S. Yoon, J.H. Jang, B.H. Ka, S.M. Oh, Complex capacitance analysis on rate capability of electric-double layer capacitor (EDLC) electrodes of different thickness, Electrochimica Acta 50 (11) (2005) 2255–2262.

[32] O. Bohlen, J. Kowal, D. Sauer, Ageing behaviour of electrochemical double layer capacitors: Part I. Experimental study and ageing model, Journal of Power Sources 172 (1) (2007) 468–475.

[33] S. Yoon, C.W. Lee, S.M. Oh, Characterization of equivalent series resistance of electric double-layer capacitor electrodes using transient analysis, Journal of Power Sources 195 (13) (2010) 4391–4399.

[34] M. Kaus, J. Kowa, D.U. Sauer, Modelling the effects of charge redistribution during self-discharge of supercapacitors, Electrochimica Acta 55 (25) (2010) 7516–7523.

[35] R. Spyker, R. Nelms, Classical equivalent circuit parameters for a double-layer capacitor, IEEE Transactions on Aerospace and Electronic Systems 36 (3) (2000) 829–836.

[36] M.Z. Bazant, K. Thornton, A. Ajdari, Diffuse-charge dynamics in electrochemical systems, Physical Review E 70 (2) (2004) 021506.

[37] L.H. Olesen, M.Z. Bazant, H. Bruus, Strongly nonlinear dynamics of electrolytes in large AC voltages, Physical Review E 82 (1) (2010) 011501.

[38] K.T. Chu, M.Z. Bazant, Nonlinear electrochemical relaxation around conductors, Physical Review E 74 (1) (2006) 011501.

[39] R. De Levie, On porous electrodes in electrolyte solutions-IV, Electrochimica Acta 9 (9) (1964) 1231–1245.

[40] J.F. Rubinson, Y.P. Kayinamura, Charge transport in conducting polymers: insights from impedance spectroscopy, Chemical Society Reviews 38 (12) (2009) 3339–3347.

[41] R. Burt, G. Birkett, X. Zhao, A review of molecular modelling of electric double layer capacitors, Physical Chemistry Chemical Physics 16 (14) (2014) 6519–6538.

[42] N. Georgi, A.A. Kornyshev, M.V. Fedorov, The anatomy of the double layer and capacitance in ionic liquids with anisotropic ions: Electrostriction vs. lattice saturation, Journal of Electroanalytical Chemistry 649 (1) (2010) 261–267.

[43] M.Z. Bazant, B.D. Storey, A.A. Kornyshev, Double layer in ionic liquids: Overscreening versus crowding, Physical Review Letter 106 (2011) 046102.

[44] C. Cagle, G. Feng, R. Qiao, J. Huang, B.G. Sumpter, V. Meunier, Structure and charging kinetics of electrical double layers at large electrode voltages, Microfluidics and Nanofluidics 8 (5) (2010) 703–708.

[45] M.V. Fedorov, A.A. Kornyshev, Towards understanding the structure and capacitance of electrical double layer in ionic liquids, Electrochimica Acta 53 (23) (2008) 6835–6840.

[46] X. Jiang, J. Huang, H. Zhao, B.G. Sumpter, R. Qiao, Dynamics of electrical double layer formation in room-temperature ionic liquids under constant-current charging conditions, Journal of Physics: Condensed Matter 26 (28) (2014) 284109.

[47] C. Merlet, B. Rotenberg, P.A. Madden, P.-L. Taberna, P. Simon, Y. Gogotsi, M. Salanne, On the molecular origin of supercapacitance in nanoporous carbon electrodes, Nature Materials 11 (4) (2012) 306–310.

[48] A.M. Johnson, J. Newman, Desalting by means of porous carbon electrodes, Journal of The Electrochemical Society 118 (3) (1971) 510–517.

[49] B. Pillay, J. Newman, The influence of side reactions on the performance of electrochemical double-layer capacitors, Journal of The Electrochemical Society 143 (6) (1996) 1806–1814.

[50] I.J. Ong, J. Newman, Double-layer capacitance in a dual lithium ion insertion cell, Journal of The Electrochemical Society 146 (12) (1999) 4360–4365.

[51] V. Srinivasan, J.W. Weidner, Mathematical modeling of electrochemical capacitors, Journal of the Electrochemical Society 146 (5) (1999) 1650–1658.

[52] C. Lin, J.A. Ritter, B.N. Popov, R.E. White, A mathematical model of an electrochemical capacitor with double-layer and faradaic processes, Journal of the Electrochemical Society 146 (9) (1999) 3168–3175.

[53] C. Lin, B.N. Popov, H.J. Ploehn, Modeling the effects of electrode composition and pore structure on the performance of electrochemical capacitors, Journal of The Electrochemical Society 149 (2) (2002) 167–175.

[54] D. Dunn, J. Newman, Predictions of specific energies and specific powers of double-layer capacitors using a simplified model, Journal of The Electrochemical Society 147 (3) (2000) 820–830.

[55] H. Kim, B.N. Popov, A mathematical model of oxide carbon composite electrode for supercapacitors, Journal of the Electrochemical Society 150 (9) (2003) 1153–1160.

[56] G. Sikha, R.E. White, B.N. Popov, A mathematical model for a lithium-ion battery/electrochemical capacitor hybrid system, Journal of the Electrochemical Society 152 (8) (2005) 1682–1693.

[57] M.W. Verbrugge, P. Liu, Microstructural analysis and mathematical modeling of electric double-layer supercapacitors, Journal of The Electrochemical Society 152 (5) (2005) 79–87.

[58] S. Kazaryan, S. Razumov, S. Litvinenko, G. Kharisov, V. Kogan, Mathematical model of heterogeneous electrochemical capacitors and calculation of their parameters, Journal of The Electrochemical Society 153 (9) (2006) 1655–1671.

[59] S.K. Griffiths, R.H. Nilson, Optimum interparticle porosity for charge storage in a packed bed of nanoporous particles, Journal of The Electrochemical Society 157 (4) (2010) 469–479.

[60] H. Wang, L. Pilon, Mesoscale modeling of electric double layer capacitors with three-dimensional ordered structures, Journal of Power Sources 221 (2013) 252–260.

[61] H. Wang, A. Thiele, L. Pilon, Simulations of cyclic voltammetry for electric double layers in asymmetric electrolytes: A generalized modified Poisson-Nernst-Planck model, Journal of Physical Chemistry C 117 (36) (2013) 18286–18297.

[62] J.H. Masliyah, S. Bhattacharjee, Electrokinetic and Colloid Transport Phenomena, John Wiley & Sons, Hoboken, NJ, 2006.

[63] G.M. Goldin, A.M. Colclasure, A.H. Wiedemann, R.J. Kee, Three-dimensional particle-resolved models of Li-ion batteries to assist the evaluation of empirical parameters in one-dimensional models, Electrochimica Acta 64 (2012) 118–129.

[64] A.H. Wiedemann, G.M. Goldin, S.A. Barnett, H. Zhu, R.J. Kee, Effects of three-dimensional cathode microstructure on the performance of Lithium-ion battery cathodes, Electrochimica Acta 88 (2013) 580–588.

[65] M.Z. Bazant, M.S. Kilic, B.D. Storey, A. Ajdari, Towards an understanding of induced-charge electrokinetics at large applied voltages in concentrated solutions, Advances in Colloid and Interface Science 152 (1-2) (2009) 48–88.

[66] M.S. Kilic, M.Z. Bazant, A. Ajdari, Steric effects in the dynamics of electrolytes at large applied voltages, II. Modified Poisson-Nernst-Planck equations, Physical Review E 75 (2) (2007) 021503.

[67] M.S. Kilic, M.Z. Bazant, A. Ajdari, Steric effects in the dynamics of electrolytes at large applied voltages, I. Double-layer charging, Physical Review E 75 (2) (2007) 021502.

[68] D. Halliday, R. Resnick, J. Walker, Fundamentals of Physics, 9th edition, John Wiley & Sons, Hoboken, NJ, 2010.

[69] H. Wang, J. Varghese, L. Pilon, Simulation of electric double layer capacitors with mesoporous electrodes: Effects of morphology and electrolyte permittivity, Electrochimica Acta 56 (17) (2011) 6189–6197.

[70] H. Wang, L. Pilon, Accurate simulation of electric double layer capacitance for ultramicroelectrodes, Journal of Physical Chemistry C 115 (33) (2011) 16711–16719.

[71] F. Booth, The dielectric constant of water and the saturation effect, Journal of Chemical Physics 19 (4) (1951) 391–394.

[72] A.J. Appleby, Electron transfer reactions with and without ion transfer, in: B. Conway, C. Vayenas, R. White, M. Gamboa-Adelco (Eds.), Modern Aspects of Electrochemistry, No. 38, Kluwer Academic/Plenum Publishers, New York, NY, 2005, pp. 175–301.

[73] G. Moumouzias, G. Ritzoulis, Relative permittivities and refractive indices of propylene carbonate + toluene mixtures from 283.15 K to 313.15 K, Journal of Chemical & Engineering Data 42 (4) (1997) 710–713.

[74] G.J. Janz, R.P.T. Tomkins, Nonaqueous Electrolytes Handbook, vol. I, Academic Press, New York, NY, 1972.

[75] J. Chmiola, G. Yushin, Y. Gogotsi, C. Portet, P. Simon, P.L. Taberna, Anomalous increase in carbon capacitance at pore sizes less than 1 nanometer, Science 313 (5794) (2006) 1760–1763.

[76] J.N. Israelachvili, Intermolecular and Surface Forces, 2nd edition, Academic Press, San Diego, CA, 1992.

[77] B. Conway, Electrolyte solutions: Solvation and structural aspects, Annual Review of Physical Chemistry 17 (1) (1966) 481–528.

[78] Y. Marcus, Ionic radii in aqueous solutions, Chemical Reviews 88 (8) (1988) 1475–1498.

[79] V. Afanas'ev, A. Ustinov, Adiabatic compressibility of hydrated complexes of electrolytes, Electrochimica Acta 54 (26) (2009) 6455–6463.

[80] M. Noked, E. Avraham, A. Soffer, D. Aurbach, Assessing the concentration effect on hydration radii in aqueous solutions by electroadsorption on a carbon molecular sieve electrode, The Journal of Physical Chemistry C 114 (31) (2010) 13354–13361.

[81] N. Nanbu, T. Ebina, H. Uno, S. Ishizawa, Y. Sasaki, Physical and electrochemical properties of quaternary ammonium bis (oxalato) borates and their application to electric double-layer capacitors, Electrochimica acta 52 (4) (2006) 1763–1770.

[82] S. Porada, G. Feng, M. Suss, V. Presser, Capacitive deionization in organic solutions: case study using propylene carbonate, RSC Advances 6 (7) (2016) 5865–5870.

[83] J. Sánchez-González, F. Stoeckli, T.A. Centeno, The role of the electric conductivity of carbons in the electrochemical capacitor performance, Journal of electroanalytical chemistry 657 (1) (2011) 176–180.

[84] L.L. Zhang, R. Zhou, X. Zhao, Graphene-based materials as supercapacitor electrodes, Journal of Materials Chemistry 20 (29) (2010) 5983–5992.

[85] H. Wang, L. Pilon, Physical interpretation of cyclic voltammetry for measuring electric double layer capacitances, Electrochimica Acta 64 (2012) 130–139.

[86] H. Wang and L. Pilon, Reply to comments on Intrinsic limitations of impedance measurements in determining electric double layer capacitances? by H. Wang and L. Pilon [Electrochimica Acta 63 (20**12) 55], Electrochimica Acta 76(0) (20**12) 529-531.

[87] D.J. Griffiths, Introduction to electrodynamics, Prentice Hall, 1962.

[88] A. S. for Metals, Metals handbook vol. 3, The Society, 1967.